Structure, Volume *22*

Supplemental Information

Determining the Oligomeric Structure of Proteorhodopsin by Gd^{3+}-Based Pulsed Dipolar Spectroscopy of Multiple Distances

Devin T. Edwards, Thomas Huber, Sunyia Hussain, Katherine M. Stone, Maia Kinnebrew, Ilia Kaminker, Erez Matalon, Mark S. Sherwin, Daniella Goldfarb, and Songi Han

Supplemental information:

1) Supplemental data:

SI 1.1) Field swept echo EPR spectra

SI 1.2) Raw DEER time domain data

SI 1.3) Estimating reliable distance limits in DEER traces

SI 1.4) Effects of background subtraction

SI 1.5) Spin-echo measurements of electron spin dephasing times

SI 1.6) Effect of multi-spin correction in DEERAnalysis

SI 1.7) Details of structural modeling

1.1) Field swept echo EPR spectra

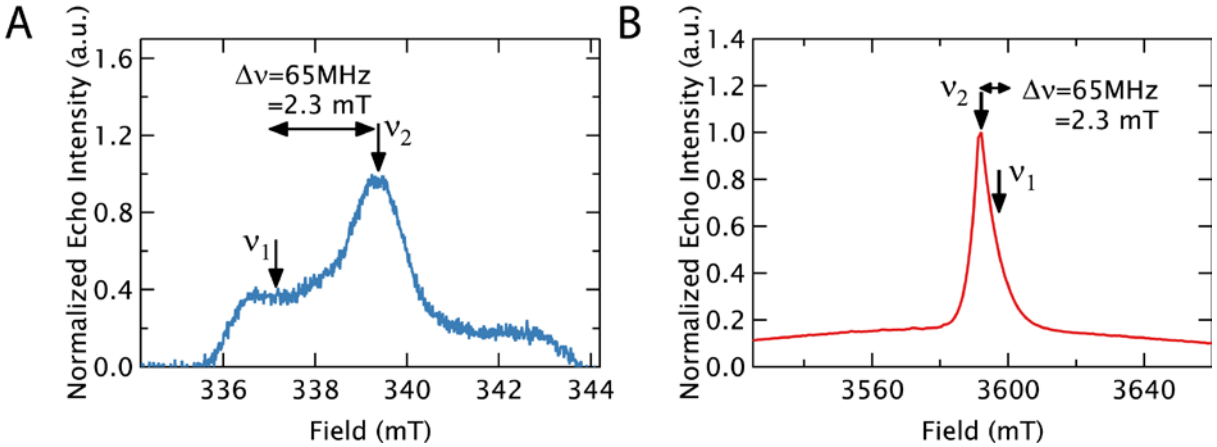

Figure S1: Locations of Pulses for DEER, Related to Figures 2 and 3. Field-swept echo EPR spectra for both 177R1 and 177G1 demonstrating the spectral locations of the typical observer (ν_1) and pump (ν_2) pulses for DEER measurements. **A**. 177R1 echo-detected spectrum at X-Band. **B**. 177G1 echo-detected spectrum at W-Band. For samples 58G1 with 33% Gd^{3+} occupancy and 177G1 with 33% and 80% Gd^{3+} occupancy ν_2 remained at the peak of the spectrum, but the spacing to ν_1 was 100 MHz≈3.5 mT.

1.2) Raw DEER time domain data

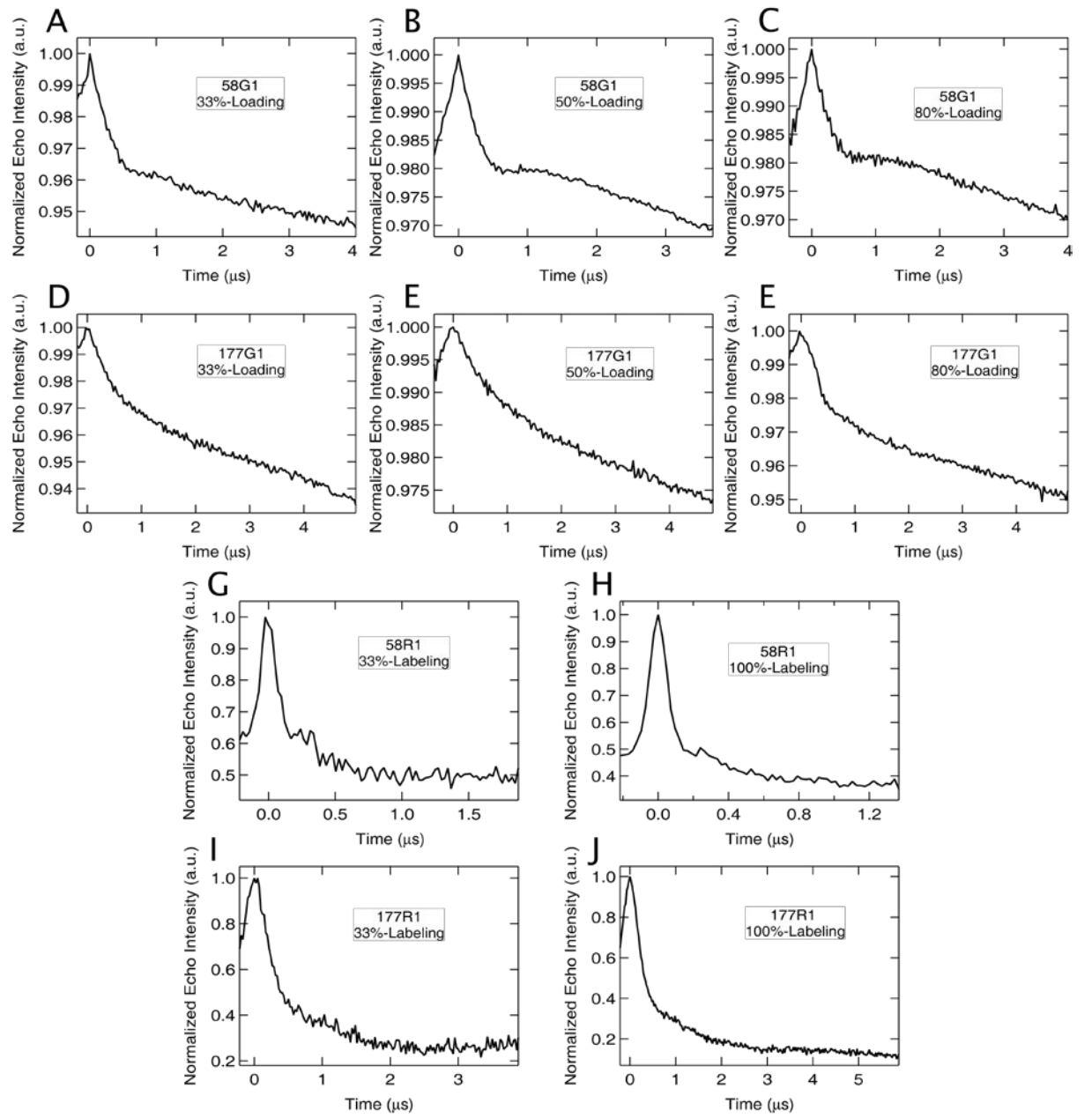

Figure S2: Raw DEER Data, Related to Figures 2 and 3. The raw (normalized) DEER data is plotted without background correction. Measurements taken at 95 GHz (i.e., for 58G1 and 177G1 (**A**, **B, C, D**, **E**, **F**)) often displays an artifact in the final ~0.5 μs resulting from the overlap of the pump pulse with the final refocusing pulse. These regions were removed from the data before any processing, and so are absent from the data plotted here.

SI 1.3) Estimating reliable distance limits in DEER traces.

Mutant	Labeling/ Loading (%)	Evolution Time (μs)	Trust Distribution Shape (nm)	Trust Mean and Width (nm)	Trust Mean Distance (nm)
58R1	100	1.368	<2.6	<3.5	<4.4
	33	1.872	<2.9	<3.9	<4.9
58G1	80	4.0	<3.8	<5.0	<6.3
	50	3.712	<3.7	<4.9	<6.1
	33	4.0	<3.8	<5.0	<6.3
177R1	100	5.88	<4.3	<5.7	<7.2
	33	3.888	<3.7	<5.0	<6.2
177G1	80	4.896	<4.0	<5.4	<6.7
	50	4.8	<4.0	<5.4	<6.7
	33	4.896	<4.0	<5.4	<6.7

Table S1: Confidence Regions of DEER Data, Related to Figures 2 and 3. Estimates of the reliability of the distance measurements based on the total dipolar evolution time for each mutant and dilution level described in the manuscript. The calculation is described in the SI 1.3.

In DEER measurements, the total dipolar evolution time (T_{evo}, corresponding to the full length of the time axis) determines the confidence in reporting long inter-spin distances and is

fundamentally restricted by the length of the electron spin phase memory time. An accepted convention (taken from the DEERAnalysis manual (Jeschke, 2013)) is that for a 2 μs evolution time the full distance distribution is reliable out to 3 nm, the assignment of a mean distance and distribution width is reliable out to 4 nm, and the mean distance value alone is reliable out to 5 nm. We can obtain reliability estimates for our DEER results by scaling these guideline distances by $\left(\frac{T_{evo}}{2\mu s}\right)^{\frac{1}{3}}$. Table S1 shows the results for each mutant and labeling level.

SI 1.4) Effects of background subtraction

The fitting of DEER time domain data can be strongly affected by the choice of the background fit to the data. Typically, a homogeneous 3-dimensional distribution of spin pairs is assumed and fit to the end of the time domain data to eliminate the signal decay due to intermolecular (or in this case, inter-oligomer) interactions (Jeschke and Polyhach, 2007). Isolating this decay from DEER oscillations (which encode the distance information) can be challenging, particularly when oscillations are weak or arise from long distances or when size exclusion effects become significant (which can result in non-exponential background decay) (Kattnig et al., 2013). For this uncertainty we wished to generate error estimates for the fitted parameters and the shapes of the distributions resulting. For all samples except 177R1 with 33% nitroxide labeling and 58G1 with 33% Gd^{3+} occupancy, we used the following approach (these other two special cases are discussed below).

Mutant	Labeling/ Loading (%)	Best r_1 (nm)	Mean r_1 (nm)	Best Δr_1 (nm)	Mean Δr_1 (nm)	Best r_2 (nm)	Mean r_2 (nm)	Best Δr_2 (nm)	Best Δr_2 (nm)
58R1	100	2.18	2.14 ±0.08	0.39	0.44 ±0.08	3.60	3.73 ±0.10	1.55	1.19 ±0.33
	33	2.40	2.40 ±0.005	0.14	0.20 ±0.04	4.21	4.12 ±0.11	1.36	1.22 ±0.24
58G1	80	2.25	2.26 ±0.01	0.32	0.32 ±0.005	3.88	3.87 ±0.01	0.63	0.61 ±0.03
	50	2.23	2.23 ±0.01	0.39	0.39 ±0.005	3.82	3.82 ±0.01	0.574	0.57 ±0.03
	30	2.27	2.24 ±0.05	0.31	0.30 ±0.01	3.86	3.85 ±0.03	0.58	0.70 ±0.22
177R1	100	3.62	3.61 ±0.01	0.70	0.67 ±0.02	5.73	5.66 ±0.05	2.22	2.07 ±0.10
	33	3.70	3.70 ±0.01	0.39	0.75 ±0.04	5.72	5.71 ±0.03	0.24	0.45 ±0.05
177G1	80	3.91	3.95 ±0.05	0.51	0.56 ±0.06	5.49	5.57 ±0.10	1.08	1.27 ±0.22
	50	3.93	3.99 ±0.06	1.0	1.30 ±0.03	6.05	6.22 ±0.17	0.87	1.22 ±0.38
	33	3.72	3.73 ±0.03	0.75	0.88 ±0.02	5.52	5.54 ±0.05	0.93	1.10 ±0.28

Table S2: Distance Results Comparisons, Related to Figures 2 and 3. The center (r_1 and r_2) and width (Δr_1 and Δr_2) of the two Gaussian distributions determined from DEER experiments for each mutant and labeling/loading level. The results from the background subtraction that gave the smallest RMSD for the fit are labeled as "Best." The average values and 1σ standard deviations from averaging the results of all background subtractions (excluding those pared as described in the SI section 1.4) are labeled as "Mean."

The starting point for fitting the 3-dimensional, homogeneous background decay was varied in steps of 100 ns across a range of reasonable values. Each resulting background-subtracted, time domain signal, was fit to the 2-component, Gaussian model. The choice of

background subtraction that resulted in a distance distribution with the smallest root-mean-square deviation (RMSD) from the time domain data (i.e., the best fit) was then selected as the best-fit distribution. These are the distributions shown in solid lines in Figs. 2C, 2D, 3C, and 3D. The remaining distributions were then evaluated with the following two criteria. Distributions were discarded if their RMSD from the data exceeded 115% of the RMSD value from the best-fit distribution. Further, to eliminate occasional outliers, distributions whose $\kappa = \frac{r_2}{r_1}$ values differed by more than 15% (i.e., from 85% to 115%) from the mean value of κ were also discarded. The distributions that remained were then averaged to generate a mean distribution, as well as standard deviations (1σ) for each point, as listed in table S2. These are the distributions and errors bars presented with the shaded regions in Figs. 2 and 3.

177R1 with 33% labeling could be well fit using a 2-component Gaussian model, but the width of the r_2 distance distribution was unphysically narrow. This was avoided by using the Tikhonov regularization to fit the time-domain data. The resulting distribution was then fit by a two-component, Gaussian model to determine values for r_1, r_2, and the relative populations and widths of each component. To account for the error in the background determination with this approach, we used the validation tool built into the DEERAnalysis (Jeschke, 2013; Jeschke et al., 2006). This tool was used to generate 50 different starting points for background fitting, and the resulting Tikhonov regularization calculated. Again we discarded curves with RMSD values more than 115% of the smallest RMSD value. The resulting Tikhonov regularization with accompanying error bars were then taken from the DEERAnalysis. Because the error bars from DEERAnalysis are 2σ error bars, they were divided by 2 to match those derived for the other samples. The errors for the parameters for the 2-component Gaussian model were estimated from fitting the mean, upper, and lower confidence level distributions.

The 58G1 with 33% Gd^{3+} occupancy could not be fit well using a purely homogeneous 3-dimensional model. Instead, the polynomial background fitting in DEERAnalysis was used. Similar effects have been seen in other studies resulting from excluded volume effects (Kattnig et al., 2013), thought there is no clear reason why this was necessary only for this data set. A 3^{rd}-order polynomial was used for the fit of the background decay, but the error estimation method was identical to that used for the other traces (except the 33%-labeled 177R1).

The extracted distance distributions with the smallest RMSD errors (the "best-fit" distributions) generally agreed well with the distribution generated from averaging the distributions from all valid backgrounds (the "mean-fit" distributions). This can be seen in Figs. 2B, 2D, 3B, 3D presented in the manuscript. There are cases where portions of the best-fit distribution fall outside the 1σ confidence range of the mean-fit distribution (for instance 58R1 with 33% nitroxide labeling). However, the determined values for r_1 and r_2 still closely agree. This can be seen in Table S2, where the r_1 and r_2 distances and the width of each (Δr_1 and Δr_2) are compared.

A comparison of the distributions also clearly indicates that the dramatic differences between the 33% and 100% nitroxide-labeled samples are not the result of the choice of background. For both 58R1 and 177R1 the mean-fit distributions show the same qualitative changes when the degree of the nitroxide labeling is changed. By contrast, as the Gd^{3+} occupancy is changed between 33% and 100%, smaller changes are observed in the distributions for 58G1 and 177G1. Further, in many cases the confidence estimates for different Gd^{3+} occupancy levels overlap, suggesting that much of the difference may be related to properly isolating the background. One exception is 80% occupied 177G1, which shows a much stronger r_1 peak than the 33% and 50% occupied samples. Though the background variation accounts for

some difference, it is not sufficient to fully explain this discrepancy. The absence of this effect in the 58G1 mutants, which possesses significantly shorter inter-spin distances, suggests that this does not result from multi-spin effects. Instead, the most likely cause is an inability to separate the background decay from the dipolar oscillation expected from the r_2 distance, causing a muting of the r_2 distance.

In evaluating the r_2 distance for 177G1 and 177R1, we consistently measure distances between 5.5 nm-6.0 nm instead of the 6.5 nm-7.0 nm expected from the modeling. This results in a value of $\kappa_{177} \sim 1.5 - 1.6$, which differs significantly from the expected value of 1.73. The mean-fit distributions do not show a significantly different r_2 value. Thus, this shorter r_2 distance does not appear to be an artifact of data processing or the choice of background. Instead, the difference must result from either a physical difference in the oligomeric structure (that is, that the r_2 distance is genuinely shorter than the model predicts) or an experimental artifact. Though we do not rule either out, a hint may be provided from with the results obtained when using the multi-spin correction in SI 1.6. Upon application of the analytic multi-spin correction to the data for 100% nitroxide labeled 177R1, the r_2 distance shifts from 5.7 nm to 6.6 nm. As discussed fully there, it is possible that the longer evolution time achieved with the 100% nitroxide-labeled 177R1 sample allowed the longer r_2 distance to be properly determined once the multi-spin effects are reduced.

SI 1.5) Spin-echo decays

Direct measurements of the 2-pulse electron spin echo decay are shown in Fig. S3 for both Gd^{3+}-labeled and nitroxide-labeled samples. Utilizing an exponential fit is challenging due to the large ^2H Electron Spin Echo Envelope Modulation (ESEEM) oscillations obscuring the 10 GHz electron spin echo decay. Instead, we record the pulse spacing that results in a decay to 10% of the maximum echo intensity ($\tau_{10\%}$). In 177R1 $\tau_{10\%}$=4.9 μs, but this drops to $\tau_{10\%}$=1.9 μs for 58R1. By contrast, the two G1-labeled mutants have similar $\tau_{10\%}$ values of 4.2 μs and 3.6 μs for 177R1 and 58R1 respectively. The site-specific relaxation times in nitroxides (Fig. S3B) result from different local environments (Jeschke, 2002; Jeschke et al., 2004). The long relaxation of 177R1 is due to its exposure to deuterated solvent (Hussain et al., 2013), compared to the buried 58R1. At this buried site, the hydrophobic nature of the nitroxide spin label may lead the nitroxide to interact with protein residues, and thus their protons. This will decrease the phase

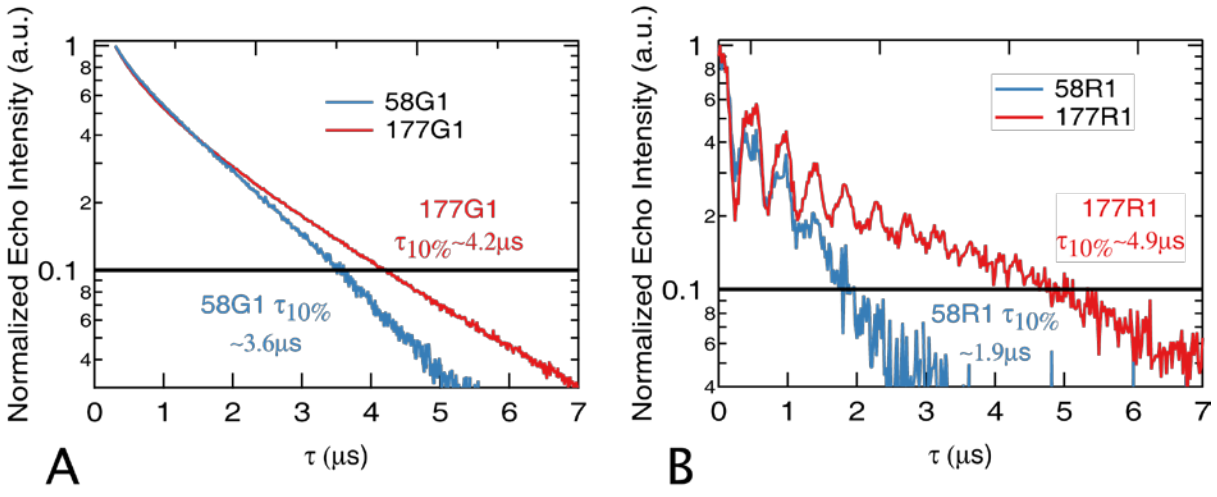

Figure S3: Echo Decay Measurements, Related to Figures 2 and 3. **A.** W-Band spin echo decay of G1-labeled PR mutants as a function of labeling position (measured at 20 K). The decay rate is largely similar for all sites; there is ~ 20% variation in the inter-pulse spacing needed to reach 10% of the initial values (shown as a black horizontal line). **B.** X-Band spin echo decay for nitroxide-labeled PR mutants as a function of labeling position (measured at 50 K). The decay rate is highly heterogeneous; there is substantial variation in the inter-pulse spacing needed to reach 10% of the initial values (shown in black). The oscillations in the spectrum are indicative of coupling to deuterium in the solvent, which disappears at high magnetic fields.

memory time (Matalon et al., 2013). In contrast, the Gd^{3+} ion in 4MMDPA can coordinate with the solvent D_2O molecules, which can shield it from the protons on the protein.

SI 1.6) Effect of multi-spin correction in DEERAnalysis

Data presented in the manuscript were not treated with numeric corrections available to offset multi-spin effects (available in the DEERAnalysis program) (von Hagens et al., 2013). The impact of this correction was tested and is presented here. Firstly, the correction shows negligible

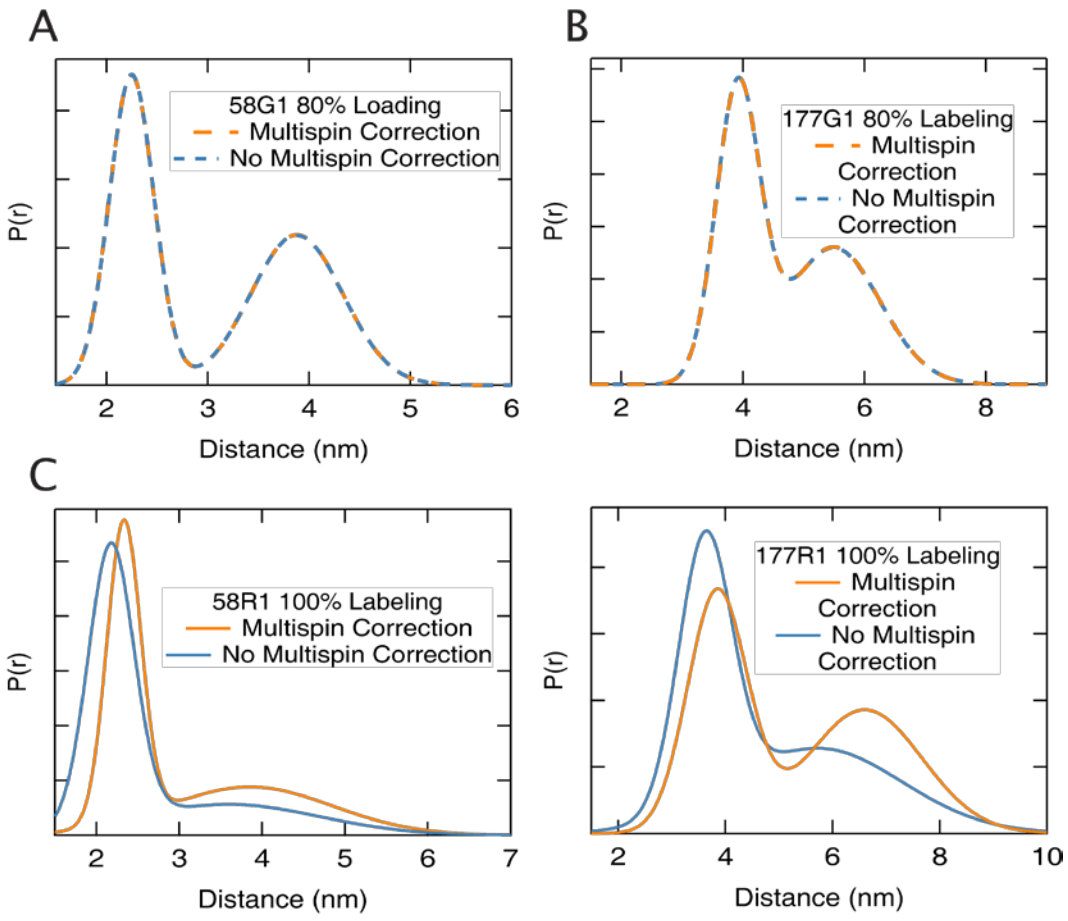

Figure S4: Effects of Analytic Multi-spin Correction, Related to Figures 2 and 3. Distance distributions (from a two Gaussian-component model) for systems with 100% of 80% spin labeling are compared with and without the multi-spin correction option in DEERAnalysis (Jeschke et al., 2006; von Hagens et al., 2013). As expected, the distance distributions are effectively identical for the G1-labeled samples (**A** and **B**) while for the R1-labeled protein the distance distributions are altered significantly with the multi-spin correction (**C** and **D**).

impact on the distance distributions for the G1-labeled samples, shown here with 80% Gd^{3+} occupancy (Figs. S3A and S3B). This is to be expected, as the modulation depth (λ) for all G1-labeled protein is very small (a few percent). Both the multi-spin effect and the numeric correction therefore do not result in meaningful changes in the distributions. By contrast, the distributions for R1-labeled protein show distinct changes in the shapes of the distributions (Figs. S3C and S3D). In both cases the r_2 distance becomes more visible with the use of the multi-spin correction. For 100%-labeled 58R1, the population ratio was allowed to vary as it was in the absence of the multi-spin correction. The use of the multi-spin correction changes the population of r_1 from 70% to 56% (close to the expected 50% value). Interestingly, there is also a noticeable shift in the r_2 distance from 5.7 nm to 6.6 nm. This longer distance is in better agreement with the distance of 6.5-7.0 nm expected from the modeling. As a result, κ_{177} shifted from 1.58 to 1.71 when using the multi-spin correction, which is nearly identical to the value of 1.73 expected for a perfect hexamer. Elimination of multi-spin effects with this analytic technique may be responsible for this shift of the r_2 distance. However, both the 33% nitroxide-labeled 177R1 samples and the 177G1 samples have significantly reduced multi-spin effects without application of this multi-spin correction. Measurements of these samples resulted in an r_2 distance significantly shorter than 6.6 nm. This difference could result from the significantly longer dipolar evolution time achieved for 100%-labeled 177R1 sample compared to other samples labeled at site 177 (5.8 μs for 100% labeled 177R1 versus ~4.8 μs for 177G1 and ~3.8 μs for 33% labeled 177R1). The shorter dipolar evolution times may explain the shorter r_2 distance, as the maximum reliable mean distances for these samples are between 6.2 nm and 6.7 nm (Table S1). In the case of 177R1 with 100% nitroxide labeling, it seems likely that that the multi-spin effects that exaggerate the r_1 distance also result in an artificial shortening of r_2. Thus, both the

multi-spin effect and a shortened dipolar evolution time may result in a coincidentally similar reduction in the observed r_2 distance. However, if a shortened dipolar evolution times were artificially shortening r_2, we might expect r_2 to be reduced further below 5.5-6.0 nm in the case of 33% nitroxide labeled 177R1, where the evolution time is the shortest. This is effect is not observed and so no strong conclusion is drawn on the likelihood of this explanation for the reduced r_2 distance in mutant 177.

SI 1.7) Details of structural modeling

Conformers were generated for each label by randomly varying the χ1 and χ2 angles of the cysteine residue as well as all rotatable bonds between the cysteine sulfur atoms and the Gd^{3+} chelating group. PyParaTools accounts for local torsion angle preferences in the attached labels by randomly sampling dihedral angles around preferred rotamer states. For example, the preferred rotamer states of a disulfide bond through which a label is attached are known to be either 90 or -90 degrees, and consequently, PyParaTools samples this torsion angle randomly

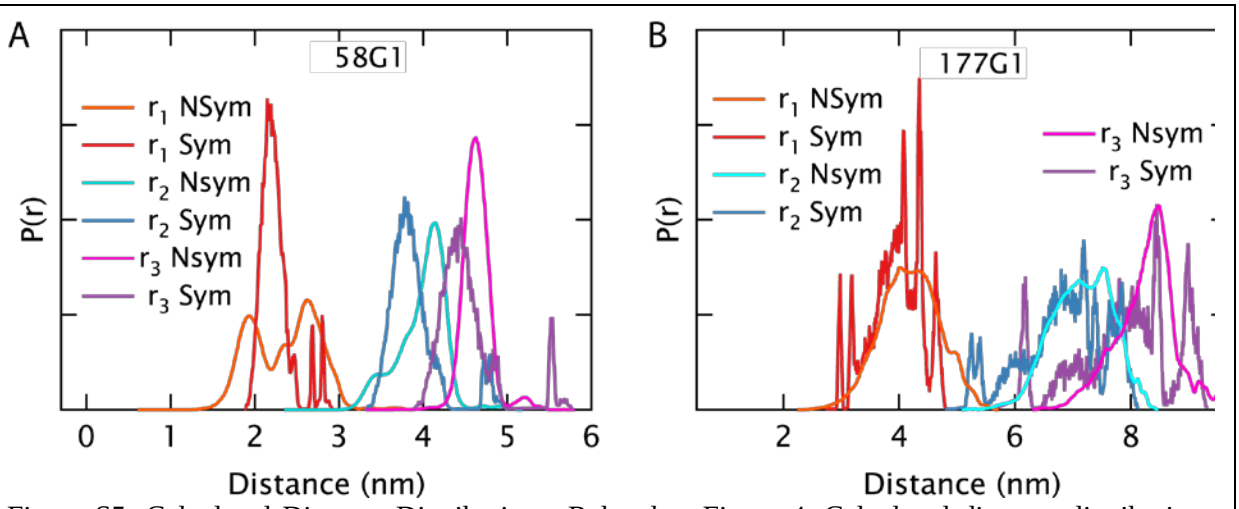

Figure S5: Calculated Distance Distributions, Related to Figure 4. Calculated distance distributions from spin labels modeled onto a homology model of G1-labeled PR. Distributions are shown for the nearest neighbor (r_1), next-nearest neighbor (r_2) and the furthest neighbor (r_3). Two different models for the tag are shown: the symmetric tag rotamers (Sym) and non-symmetric tag rotamers (Nsym). **A.** Model results for buried site 58, **B.** Model results for solvent exposed site 177.

around these values with a window size of 20 (±10) degrees. Similarly, torsions around carbon-carbon bonds are sampled from the preferred rotamer states -60±10, 60±10 and 180±10 degrees, with the exception of the last rotatable bond to the Gd^{3+} chelate, which was assumed to be restricted to -90±10 / 90±10 degrees.

Models with severe steric violations between the tags and the protein were removed. To account for possible inaccuracies in the homology, model van der Waals radii in these calculations were scaled down by one third for the buried site 58, but assumed the normal values for the solvent exposed site 177. Approximately 10000 4MMDPA-Gd^{3+} tag conformations were calculated for each site in the first subunit of the G-PR hexamer, and in all other subunits the symmetry related tag conformations were computed by satisfying symmetry restraints. Distribution were finally calculated by tallying occurrence of Gd^{3+}- Gd^{3+} distances in 0.01 nm bins for nearest and next-nearest neighbor subunits.

To assess non-symmetric tag arrangements, the distance between paramagnetic centers was also calculated for each pair-wise combination of approximately 1000 modeled tag conformations, and the resulting $>10^6$ distances were tallied into distributions with 0.01 nm bin widths. The results with and without symmetry are shown in Fig. S6 for all 3 possible inter-protein distances. For 58G1, the symmetric distributions appear to give more reasonable distance distributions. Alternatively, for 177G1 the non-symmetric distributions appear to offer better (though similar) results.

The details of the experimentally verified structural model are consistent with the distinct differences in the local environments of the labeling sites. For instance, site 58 is buried (Stone et al., 2013), which may explain why modeling suggests the tag arranges with C_6 symmetry within the G-PR hexamer. The buried position of the label at residue 58 is also

consistent with the short phase memory time observed for 58R1 that can result from exposure to protein protons that enhance spin-echo decay rates (Jeschke, 2002; Jeschke et al., 2004). In contrast, site 177 is located within a loop region between helices E and F and is solvent exposed (Hussain et al., 2013). A reasonable consequence of this flexibility is that modeling with non-symmetric rotamer confirmations best describes the measured distance distribution for 177G1.

2) Supplemental experimental procedures:

SI 2.1) Preparation of proteorhodopsin samples

Labeling of the protein with Gd^{3+} followed previous literature utilizing 4MMDPA (Potapov et al., 2010; Su et al., 2008). Briefly, after the protein was bound to a His-tag affinity resin and contaminant proteins washed away, the bound G-PR was reacted with a 30-fold excess of 5,5'-dithiobis-(2-nitrobenzoic Acid) (DTNB) in a 50 mM Tris buffer (pH 7.5) at room temperature for one hour. Free DTNB and TNB were then washed and a 4-fold excess of 4MMDPA added and allowed to react. The labeled protein was eluted in a 400 mM imidazole, 50 mM Tris buffer, containing .05 wt% of the β-dodecylmaltoside (DDM) surfactant.

For both 4MMDPA-labeled and nitroxide-labeled G-PR, the buffer was exchanged following isolation of the hexamer through size-exclusion FPLC. The solvent was exchanged to D_2O using Sephadex PD-10 desalting columns (GE Healthcare) equilibrated with 50 mM Tris

buffer made with D_2O containing 0.05 wt% DDM. This was followed by concentrating the solution using 50,000 MWCO centrifugal filters (Millipore) to a desired PR concentration.

Spin dilutions of 177R1 and 58R1 were prepared by mixing unlabeled G-PR (with no cysteine mutations) with nitroxide-labeled G-PR in 2 wt% DDM and rocking overnight at 4˚C to allow exchange of the labeled and unlabeled G-PR within the hexameric form. The sample was then diluted to a final concentration of 1% DDM to promote hexamer formation before performing the size-exclusion separation via FPLC.

Optical bsorption measurements were performed on G-PR samples to ensure that mutation and spin-labeling of the protein did not disrupt the hexameric structure. Under the conditions of the DEER experiments (50 mM Tris, D_2O, 0.05 wt% DDM), G-PR spin-labeled at the loop residue 177 displayed small red-shifts in maximum absorption (4-9 nm), suggesting some change in the retinal microenvironment, while the Trp58Cys mutation caused a larger red-shift of 17 nm. In spite of these color changes, the oligomeric distribution isolated in DDM by SEC was similar to wild-type PR. Therefore, as discussed in the main text, we conclude that the overall oligomeric structure studied here was not compromised by either mutation or spin-labeling.

SI 2.2) DEER measurements

In the case of the W-Band measurements samples were contained in 0.84 outer diameter, 0.6 inner diameter quartz capillaries with an EPR active volume of 2-3 μL. The pump pulse was centered on the maximum of the Gd^{3+} spectrum, which was also placed at center of the cavity resonance. The observer pulse was applied at a spacing of 100 MHz for the 33% 58G1, and 80% and 33% 177G1 samples but between 65-75 MHz for all other samples (see Fig. S1). The pump

π-pulse length was 15 ns and the $\frac{\pi}{2}$, π observer pulses were 15 and 30 ns, respectively. The first observer echo spacing was fixed at $\tau_1 = 400$ ns and the repetition time was 500 μs. For the W-band DEER measurements a phase cycle described in Gordon-Grossman et al. (2011) was used. In the X-Band measurements, an ER4118X-MS-5 probe head with a split ring resonator (5 mm sample access) was used with ~50-60 μL samples. The maximum of the nitroxide spectrum was placed at the center of the cavity bandwidth and used for the pump pulse, while the observer pulse was spaced by 65 MHz (see Fig. S1). The pump π-pulse length was 16 ns and the $\frac{\pi}{2}$ and π observer pulses were both 32 ns. The repetition time was set to 2.5 μs. A +x/-x phase cycle on the first pulse was employed along with averaging over 25 increments of τ_1 (τ_1 = 400 ns, $\Delta\tau_1$ = 8 ns) to suppress nuclear modulations.

Supplementary References:

Jeschke, G. (2002). Distance Measurements in the Nanometer Range by Pulse EPR. ChemPhysChem *3*, 927-932.

Jeschke, G., Bender, A., Paulsen, H., Zimmermann, H., and Godt, A. (2004). Sensitivity enhancement in pulse EPR distance measurements. Journal of Magnetic Resonance *169*, 1-12.

Kattnig, D.R., Reichenwallner, J., and Hinderberger, D. (2013). Modeling Excluded Volume Effects for the Faithful Description of the Background Signal in Double Electron–Electron Resonance. The Journal of Physical Chemistry B *117*, 16542-16557.